Mid-Infrared Spectral Diagnostics of Nuclear and Extra-Nuclear Regions in Nearby Galaxies

D.A. Dale[1], J.D.T. Smith[2], L. Armus[3], B.A. Buckalew[3], G. Helou[3], D.J. Hollenbach[4],

T.H. Jarrett[3], R.C. Kennicutt[5,2], L.J. Kewley[6], C. Leitherer[7], J. Moustakas[2], E.J. Murphy[8],

H. Roussel[3], K. Sheth[3], et al.

ABSTRACT

Mid-infrared diagnostics are presented for a large portion of the Spitzer Infrared Nearby Galaxies Survey (SINGS) sample plus archival data from the *Infrared Space Observatory* and the *Spitzer Space Telescope*. The SINGS dataset includes low- and high-resolution spectral maps and broadband imaging in the infrared for over 160 nuclear and extranuclear regions within 75 nearby galaxies spanning a wide range of morphologies, metallicities, luminosities, and star formation rates. Our main result is that these mid-infrared diagnostics effectively constrain a target's dominant power source. The combination of a high ionization line index and PAH strength serves as an efficient discriminant between AGN and star-forming nuclei, confirming progress made with *ISO* spectroscopy on starbursting and ultraluminous infrared galaxies. The sensitivity of *Spitzer* allows us to probe fainter nuclear and star-forming regions within galaxy disks. We find that both star-forming nuclei and extranuclear regions stand apart from nuclei that are powered by Seyfert or LINER activity. In fact, we identify areas within three diagnostic diagrams containing $\gtrsim 90\%$ Seyfert/LINER nuclei or $\gtrsim 90\%$ H II regions/H II nuclei. We also find that, compared to starbursting nuclei, extranuclear regions typically separate even further from AGN, especially for low-metallicity extranuclear environments. In addition, instead of the traditional mid-infrared approach to differentiating between AGN and star-forming sources that utilizes relatively weak

[1]Department of Physics and Astronomy, University of Wyoming, Laramie, WY 82071; ddale@uwyo.edu

[2]Steward Observatory, University of Arizona, 933 North Cherry Avenue, Tucson, AZ 85721

[3]California Institute of Technology, MC 314-6, Pasadena, CA 91101

[4]NASA/Ames Research Center, MS 245-6, Moffett Field, CA 94035

[5]Institute of Astronomy, University of Cambridge, Madingley Road, Cambridge CB3 0HA, United Kingdom

[6]Institute for Astronomy, 2680 Woodlawn Drive, Honolulu, HI 96822

[7]Space Telescope Science Institute, 3700 San Martin Drive, Baltimore, MD 21218

[8]Department of Astronomy, Yale University, New Haven, CT 06520

high-ionization lines, we show that strong low-ionization cooling lines of X-ray dominated regions like [Si II] 34.82 μm can alternatively be used as excellent discrimants. Finally, the typical target in this sample shows relatively modest interstellar electron density (~ 400 cm^{-3}) and obscuration ($A_V \sim 1.0$ mag for a foreground screen), consistent with a lack of dense clumps of highly obscured gas and dust residing in the emitting regions.

Subject headings: infrared: galaxies — infrared: ISM

1.   Introduction

The goal of this study is to explore whether mid-infrared diagnostics developed for luminous/ultraluminous infrared galaxies and bright Galactic H II regions can be improved upon and extended to the nuclear and extra-nuclear regions within normal and infrared-faint galaxies. A traditional method for characterizing a galaxy's nuclear power source uses ratios of optical emission lines such as [O II] 3727Å, Hβ 4861Å, [O III] 5007Å, [O I] 6300Å Hα 6563Å, [N II] 6584Å and [S II] 6716,6731Å (e.g., Baldwin, Phillips, & Terlevich 1981; Veilleux & Osterbrock 1987; Kewley et al. 2001; Kauffmann et al. 2003). A plot of [O III]/Hβ versus [N II]/Hα, for example, will typically separate Seyferts, LINERS, and starburst nuclei. Since nuclei are often heavily enshrouded by dust, especially in luminous and ultraluminous infrared galaxies (LIRGs and ULIRGs), an important limitation to galaxy optical diagnostics is the effect of extinction. In anticipation of the data stream from space-based infrared platforms, early theoretical work with photoionization models showed that infrared ionic fine structure line ratios could profitably enable astronomers to approach galaxy classification from a new perspective (e.g., Voit 1992; Spinoglio & Malkan 1992). The advent of sensitive infrared line data from the *Infrared Space Observatory* was an important first step to peering more deeply into buried nuclear sources (Genzel et al. 1998; Laurent et al. 2000; Sturm et al. 2002; Peeters, Spoon, & Tielens 2004). Genzel and collaborators were the first to show that ionization-sensitive indices based on mid-infrared line ratios correlate with the strength of polycyclic aromatic hydrocarbon (PAH) emission features. AGN in particular show weak PAH and large ratios of high-to-low ionization line emission. High ionization lines are not the only route, though, to determining whether a galaxy harbors a strong AGN. Similar to how the [O I] 6300Å line is an AGN diagnostic, the [O I] 63 μm far-infrared line can also help to decipher a galaxy's power source (Dale et al. 2004a). Interestingly, the Genzel et al. study found that 70-80% of their ULIRG sample is mainly powered by starburst activity, yet optical studies typically show a much smaller percentage of ULIRGs powered by star formation (e.g., Veilleux, Sanders, & Kim 1999). Taniguchi et al. (1999) address this discrepancy by suggesting that the nuclei of LINER-like ULIRGs are in fact dominated by shocks driven by powerful supernova winds. Mid-infrared lines observed by *ISO* were also used to probe the physical characteristics and evolution of purely starbursting nuclei (Thornley et al. 2000; Verma et al. 2003) and Galactic H II regions (Vermeij & van der Hulst 2002; Giveon et al. 2002). An important result stemming from these efforts is that stellar aging effects

appear to result in H II regions generally having higher excitations than starbursting nuclei.

The unprecedented sensitivity and angular resolution afforded by the *Spitzer Space Telescope* allow even more detailed studies of galaxy nuclei (e.g., Armus et al. 2004; Smith et al. 2004). SINGS takes full advantage of *Spitzer*'s capabilities by executing a comprehensive, multi-wavelength survey of 75 nearby galaxies spanning a wide range of morphologies, metallicities, luminosities, and star formation activity levels. The sensitivity of *Spitzer* coupled with the proximity of the SINGS sample allows dwarf galaxy systems fainter than $L_{\rm FIR} \sim 10^7 \; L_\odot$ to be spectroscopically probed in the infrared for the first time. In addition, prior to *Spitzer* the only individual extragalactic H II regions that were detectable with infrared spectroscopy resided in the Local Group (e.g., Giveon et al. 2002; Vermeij et al. 2002). In contrast, SINGS provides infrared spectroscopic data for nearly 100 extragalactic H II regions, residing in systems as near as Local Group members to galaxies as far as $\sim$25 Mpc. The SINGS dataset thus samples a wider range of environments than previously observed with infrared spectroscopy. This diversity in the SINGS sample provides a huge range for exploring physical parameters with the mid-infrared diagnostics presented below.

2. The Sample

2.1. Galaxy Nuclei

The sample of nuclear targets analyzed in this study derive from the SINGS Third Data Release. These 50 nuclei come from a wide range of environments and galaxies: low-metallicity dwarfs; quiescent ellipticals; dusty grand design spirals; Seyferts, LINERs, and starbursting nuclei of normal galaxies; and systems within the Local and M 81 groups.

2.2. Extra-Nuclear Regions

The 26 extranuclear sources studied in this work also come from the SINGS Third Data Release. These targets stem from the original set of 39 optically-selected sources listed in Kennicutt et al. (2003). The optically-selected OB/H II regions cover a large range of metallicity (0.1-3 $Z_\odot$), extinction-corrected ionizing luminosity ($10^{49} - 10^{52}$ photons s^{-1}), extinction ($A_V \lesssim 4$ mag), radiation field intensity (ionization parameter $\log U = -2$ to -4), ionizing stellar temperature ($T_{\rm eff} = 35 - 55$ kK), and local H_2/H I ratio as inferred from CO ($<$0.1 to $>$10). Additional extranuclear targets for the SINGS project have since been identified, based on their infrared properties, but their observations necessarily came later than the observations of the optically-selected targets. Those "Second Look" data will be the focus of a future paper.

3. The Data

The full SINGS observing program and the data processing are described in Kennicutt et al. (2003), Smith et al. (2004), and Dale et al. (2005). Here we briefly summarize the spectral observations and data processing relevant to this paper.

3.1. *Spitzer* Infrared Spectroscopy Observations and Data Processing

High-resolution spectroscopy ($R \sim 600$) was obtained in the Short-High (10-20 μm) and Long-High (19-38 μm) modules, and low-resolution spectroscopy ($R \sim 50 - 100$) was obtained in the Short-Low (5-14 μm) and Long-Low (14-38 μm) modules (Houck et al. 2004a). Figure 1 shows example spectra for a variety of sources (Long-Low data are not used elsewhere in this work). Nuclei were generally mapped with a 3×5 grid (Short-High and Long-High) and a 1×18 grid (Short-Low), utilizing half-slit width and half-slit length steps. Extra-nuclear targets were observed with a similar scheme but with a 1×9 Short-Low grid. For a subset of nine sources with extended circumnuclear star formation we obtained slightly larger (6×10) Short-High nuclear maps. Owing to the different angular sizes subtended by the instruments, the resulting maps are approximately $57''\times31''$ and $57''\times18''$ in Short-Low (nuclear and extra-nuclear, respectively), $45''\times33''$ in Long-High, and $23''\times15''$ in Short-High (the 10 expanded Short-High nuclear maps are $40''\times28''$). All integrations are 60 s per pointing, except the Short-Low nuclear maps are 14 s per pointing. The effective integrations are longer since each location was covered 2-4 times.

The individual data files for a given spectral map were assembled into spectral cubes using the software CUBISM (Kennicutt et al. 2003; Smith et al. 2006, in preparation). The cube input data were pre-processed using version S12.0 of the *Spitzer Science Center* pipeline. Various post-processing steps within CUBISM are described in Smith et al. (2004). Short-Low sky subtraction was enabled via the extended off-source wings of the Short-Low module (and occasionally using spatially- and temporally-proximate data from the archive when our off-source wings do not extend to the sky). Several cross-checks on the flux calibration were made between Short-Low, Short-High, Long-Low, Long-High, MIPS, and IRAC data. The absolute flux calibration uncertainty for the spectral data is estimated to be 25%; the uncertainy in line flux ratios is $\sim$10%.

Though the Short-High, Long-High, and Short-Low cubes all span different solid angles, the same matched extraction apertures were used for all cubes: one-dimensional spectra were extracted from the three-dimensional data using $\sim23''\times15''$ apertures. Furthermore, the extraction apertures are centered on the optically-derived coordinates listed in Kennicutt et al. (2003); in general, the apertures are centered on infrared-bright emission regions. Emission line and PAH feature fluxes and equivalent widths are derived from continuum-subtracted Gaussian fits to the lines and first- or second-order fits to the continua.

3.2. Archival Spectroscopy

ISO-SWS and *Spitzer* IRS line fluxes are drawn from the literature for a wide variety of sources including Galactic, Magellanic Cloud, and Local Group H II regions (Vermeij et al. 2002; Giveon et al. 2002; Peeters et al. 2002), and starburst and active galaxies (Genzel et al. 1998; Sturm et al. 2002; Verma et al. 2003; Armus et al. 2004; Peeters, Spoon, & Tielens 2004; Weedman et al. 2005; Haas et al. 2005). Equivalent widths of the 6.2 μm PAH feature were extracted from archival *ISO*-PHOT and *Spitzer* IRS data, when available. Note that, for a given source, only data from *Spitzer* or only data from *ISO* are used; cross-observatory data are not used in this analysis. The field-of-view of the *ISO*-PHOT aperture, $24'' \times 24''$, provides a decent match to the $\sim 23'' \times 15''$ Short-High extraction apertures described in § 3.1.

3.3. *Spitzer* Broadband Imaging: 24 μm

We do not obtain nearby sky observations in HighRes mode, so if the the underlying hot dust continuum emission is detected, the foreground/background continuum is not subtracted. SINGS IRS HighRes spectroscopy is designed to measure line *fluxes* and thus line equivalent width measures via HighRes are biased by the un-subtracted sky emission. On the other hand, the SINGS program includes extensive MIPS (Rieke et al. 2004) 24 μm broadband imaging of all galaxies; the 24 μm data can be used to normalize line fluxes. Sky-subtracted MIPS 24 μm fluxes are extracted from aperture cutouts matched to the Short-High field-of-view (§ 3.1). See Kennicutt et al. (2003) and Dale et al. (2005) for further details of the SINGS broadband imaging.

3.4. Optical Spectroscopy Observations and Data Processing

Optical spectrophotometry has been obtained for the SINGS project at the Steward Observatory Bok 2.3 m and the CTIO 1.5 m telescopes (Moustakas & Kennicutt 2006). A suite of spectral drift scans, centered on the nuclei, were taken to spatially map the various regions covered with the IRS spectroscopy program (see Kennicutt et al. 2003 for more details). The optical spectroscopy has spectral resolution of ~ 8Å and covers 3600-7000Å so that the primary nebular emission lines can be studied (e.g., [O II] 3727Å, Hβ 4861Å, [O III] 5007Å, Hα 6563Å, [N II] 6584Å).

This work utilizes optical spectral drift scans integrated over the central $20'' \times 20''$ regions, approximately matching the $\sim 23'' \times 15''$ circumnuclear regions over which the infrared line and PAH feature fluxes are extracted (see § 3.1).

4. Measured Quantities

4.1. High-Resolution Infrared Spectroscopy: Emission Lines

Several forbidden lines are quite prominent in many of the SINGS nuclear and extra-nuclear high resolution spectra ([Ne II]12.81 μm, [Ne III]15.56 μm, [S III]18.71 μm, [S III]33.48 μm, and [Si II]34.82 μm) along with a few other higher ionization lines that are occasionally observed ([S IV]10.51 μm, [Ne V]14.32 μm, and [O IV]25.89 μm; Figure 1). All these lines except [Si II]34.82 μm are nebular lines from hydrogen gas ionized regions; [Si II]34.82 μm comes from a wider variety of regions, including both ionized gas and warm atomic gas such as photo-dissociation regions and X-ray dominated regions (e.g., Hollenbach & Tielens 1999). A series of interstellar molecular hydrogen lines are also detected in the SINGS spectra; these are explored in a separate paper (Roussel et al. 2006, in preparation). The line fluxes utilized in this work are listed in Tables 1 and 2. Eight galaxies from the SINGS Third Data Release are not listed in Table 1 because their nuclear regions were too faint to be observed (or detected if observed).

4.2. Low-Resolution Infrared Spectroscopy: The 6.2 μm PAH Feature

The strength of a PAH feature depends on a complex combination of several parameters of the interstellar medium, some of which are interlinked: metallicity, dust column density, the distribution of sizes and ionization states in the dust grain population, and the intensity and hardness of the interstellar radiation field (e.g., Cesarsky et al. 1996; Thuan et al. 1999; Sturm et al. 2000; Li & Draine 2001; Draine & Li 2001; Houck et al. 2004b; Galliano et al. 2005; Engelbracht et al. 2005). Due to this sensitivity to the properties of the interstellar medium, PAH features in the mid-infrared have been used to characterize the physical state of the gas in photo-dissociation regions. Previous efforts have utilized the 6.2 μm feature (Laurent et al. 2000; Peeters, Spoon, & Tielens 2004; Weedman et al. 2005), the 7.7 μm feature (Genzel et al. 1998), or a combination of several PAH features (e.g., Verstraete et al. 2001; Tran et al. 2001; Peeters et al. 2002; Förster Schreiber et al. 2004; Armus et al. 2004; Peeters et al. 2004; Madden et al. 2005). For this work we concentrate on diagnostics that utilize the 6.2 μm feature. The 6.2 μm feature is the only strong infrared signature of PAHs not blended with an emission line or absorption trough, not near the wavelength edges of an IRS low resolution module, and for which the blue and red sides of the continuum are easy to define. The equivalent widths of the 6.2 μm feature are listed in Tables 1 and 2. The equivalent width is used in our diagnostics since the continuum at 6.2 μm contains emission from either hot dust from star formation or an AGN; the 6.2 μm equivalent width is (indirectly) sensitive to the presence of an AGN.

5.   Results

5.1.   Optical Classifications of Nuclei

Not all of the SINGS galaxies have an optical nuclear classification in the literature (e.g., Seyfert, LINER, starburst, etc). Moreover, online databases such as NED[1] provide a heterogeneous source for such classifications. Thus we turn to our own optical spectroscopy. Figure 2 displays a traditional diagnostic diagram (e.g., Baldwin, Phillips, & Terlevich 1981) using optical spectroscopy and $20'' \times 20''$ apertures for SINGS galaxy nuclei. Filled (open) circles in Figure 2 mark galaxies for which the literature indicates a Seyfert (LINER) nucleus; data points without circles in this diagram represent galaxies without a LINER or Seyfert classification in the literature. As alluded to in § 1, the LINER classification can be complicated. Similar to what is observed for Seyferts, the optical properties of LINERs are consistent with a hard power-law spectrum. But LINER-type spectra can also be produced via winds, shocks, and cooling flows (Kauffmann et al. 2003). To further complicate the picture, "transition" objects are thought to be LINER or Seyfert galaxies with substantial contributions from normal star formation (e.g., Ho, Filippenko, & Sargent 1993).

The dotted lines delineate typical starburst/AGN/LINER boundaries: [O III]5007/H$\beta \sim 5$ and [N II]6583/H$\alpha \sim 0.6$ (e.g., Veilleux & Osterbrock 1987; Armus, Heckman, & Miley 1989). The long-dashed curve traces the theoretical starburst/AGN boundary of Kewley et al. (2001), marking the maximum position in this diagram that can be obtained by pure photoionization. Objects lying above this curve require an additional power source such as an AGN or shocks; objects lying below this curve may still contain an AGN responsible for up to $\sim$30% of the emission line flux ratios. The short-dashed curve traces an empirical starburst/AGN boundary based on data from tens of thousands of Sloan Digital Sky Survey galaxies (Kauffmann et al. 2003). The Kauffman et al. curve aims to define a boundary below which no galaxies contain an AGN. Objects lying in between the Kewley et al. and the Kauffmann et al. curves are likely to be composite AGN/starburst objects but still dominated by star formation. It is evident that the classification information available from the literature is insufficient or incomplete for a handful of SINGS nuclei; there is overall good agreement between the literature and our classifications, with a few exceptions. The literature does not indicate that the nuclei of NGC 1291 contains LINER or Seyfert activity, whereas our spectroscopic data place it squarely in the LINER category. On the other hand, NED lists NGC 1097, NGC 4321, and NGC 4552 as having LINER or Seyfert nuclei, yet our optical line ratios suggest they are star-forming galaxies. NGC 3198, NGC 3621, and NGC4826 appear to lie in a transitional regime between the starburst and LINER/Seyfert regions.[2]

Using the Hα/Hβ ratio extracted from our optical spectra and a screen model for the dust distribution within a galaxy, the SINGS nuclei show modest attenuations, $\langle A_V \rangle \sim 1.0$ mag with a

---

[1]NASA/IPAC Extragalactic Database

[2]Similar results are found using [S II] 6716,6731Å and [O I] 6300Å data in place of [N II] 6584Å (e.g., Kewley et al. 2001).

dispersion of 1.0 mag and a maximum of $A_V \sim 4.1$ mag for NGC 1266. No sources appear to be heavily buried in the optical so presumably none of the classifications are skewed by large amounts of dust.[3] However, as described above, there may be a few transitional objects for which the nuclear classifications are difficult to interpret in the optical. The main reason behind the analysis in this section is to provide classifications for sources that do not yet have them from the literature. Our goal is not to carry out a detailed analysis of the relative merits of classifying in the optical versus in the infrared, primarily since the SINGS sample is not optimally suited for such a test. In the next section we turn to exploring new and existing infrared diagnostics.

5.2. Infrared Diagnostics of Nuclei and Extra-Nuclear Regions

5.2.1. Emission Line Ratios and PAH Strength

The ionization potential of [O IV] is 54.9 eV. Consequently, photons at least this energetic are required to remove an electron from doubly-ionized oxygen. On the other hand, ionizing neutral neon "only" requires 21.6 eV. Compared to 21.6 eV photons, 54.9 eV photons are far more likely to stem from accretion-powered disks than star formation (e.g., OB stars; Smith et al. 2004), and thus the ratio of [O IV]25.89 μm and [Ne II]12.81 μm depends on the type of source dominating the energetics of the interstellar medium. Furthermore, studies show that PAH features are quite prominent throughout much of the interstellar medium except for regions characterized by exceptionally hard radiation fields such as those that arise in AGN and the cores of H II regions (Cesarsky et al. 1996; Sturm et al. 2000). A mid-infrared diagnostic diagram first put forth by Genzel et al. (1998), and later explored by Peeters, Spoon, & Tielens (2004), plots the emission line ratio [O IV]25.89 μm/[Ne II]12.81 μm versus the strength of a mid-infrared PAH feature. In such plots AGN sources show enhanced [O IV]25.89 μm emission and comparatively weak PAH feature strength. However, those two studies focussed on AGN-dominated and starburst nuclei. The upper panel of Figure 3 uses the 6.2 μm PAH feature and the emission line ratio [O IV]25.89 μm/[Ne II]12.81 μm in a similar mid-infrared diagnostic diagram, but one that incorporates "normal" (starbursting/star-forming) nuclei and H II regions—the sensitivity of *Spitzer* allows us to probe to far fainter levels than heretofore possible. As expected, normal nuclei and H II regions extend the previously-observed trend: lower-luminosity star-forming nuclei and H II regions exhibit comparatively large 6.2 μm equivalent widths and relatively low ratios of [O IV]25.89 μm/[Ne II]12.81 μm, indicating strong contributions from [Ne II]12.81 μm cooling of H II regions and their PAH-rich photo-dissociation region surroundings, and negligible emission from AGN.

High ionization lines like [O IV]25.89 μm are somewhat difficult to detect in many SINGS

---

[3]The exception is NGC 1377, a deeply obscured system for which the optical data are likely probing only foreground emission (Roussel et al. 2003).

sources. An alternative diagnostic diagram is provided in the lower panel of Figure 3 involving the more easily detectable [Si II] 34.82 μm line. Why are similar trends seen in the two panels? The answer may lie in the physics of X-ray dominated regions. As pointed out by Maloney, Hollenbach, & Tielens (1996), the [Si II]34.82 μm line is a strong coolant of X-ray irradiated gas. In X-ray dominated regions the X-ray emission dominates that from the comparatively small H II-like regions surrounding the hard-spectrum source. Moreover, X-ray dominated regions can be quite large since hard X-ray photons penetrate large column densities, and the conversion of X-ray energy to infrared continuum and line emission can be very efficient. Maloney, Hollenbach, & Tielens (1996) predict that [Si II]34.82 μm, [O I]63 μm, [C II]158 μm, and [C I]609 μm are the top four cooling lines within X-ray dominated regions, with [Si II]34.82 μm having an amplitude 1-10% that of the far-infrared luminosity for an extremely large range of physical conditions.

An argument based on interstellar density provides another possibility for the high [Si II]34.82 μm/[Ne II]12.81 μm ratio in AGN. Kaufman et al. (2006, in preparation) show that the ratio [Si II](PDR)/[Si II](H II) increases with increasing density. In fact, for low density H II regions most of the [Si II] comes from the H II region and not the surrounding photo-dissociation region. Moreover, Meijerink & Spaans (2005) show that the ratio [Si II](XDR)/[Si II](PDR) also increases with increasing density. AGN may have their emitting gas at higher densities than typically found in starbursts and normal galaxies, leading to an increased [Si II]34.82 μm/[Ne II]12.81 μm ratio. In other words, if the [Si II] comes mostly from X-ray dominated regions, then the high [Si II]34.82 μm/[Ne II]12.81 μm for AGN sources is due to strong [Si II] cooling. If most of the [Si II] emission comes from photo-dissociation regions, then the high [Si II]34.82 μm/[Ne II]12.81 μm for AGN sources is due to enhanced [Si II] emission in dense photo-dissociation regions.

If the strong [Si II]34.82 μm emission is due to X-ray dominated regions and not dense photo-dissociation regions, it should be noted that relatively strong low-ionization line emission (e.g., [O I] 6300Å and [O I]63 μm) has previously been observed emanating from the large "partially-ionized regions" surrounding AGN and infrared-bright galaxies (Veilleux & Osterbrock 1987; Armus, Heckman, & Miley 1989; Veilleux 1991; Spinoglio & Malkan 1992; Osterbrock 1993; Dale et al. 2004a). Hence, strong low-ionization line emission from AGN is not a new concept. We take advantage of this concept to present a new technique for distinguishing between AGN sources and star-forming regions. This technique relies on an easily-detectable, prominent cooling line of a low-ionization species associated with X-ray dominated regions, the dense interstellar material illuminated by power-law radiation fields.

In both panels of Figure 3 the region where Seyferts/LINERs/starbursts mix is quite large; only the top left and bottom right extremes allow for a clean separation between classifications. Seyfert nuclei could shift toward the location of star-forming nuclei due to aperture effects—though the same solid angles are used for extracting the line data, the range of distances in the sample leads to a range in physical apertures. Conversely, some star-forming nuclei exhibit relatively large line ratios and small PAH equivalent widths in Figure 3. Perhaps a fraction of the star-forming regions contain significant numbers of Wolf Rayet stars, leading to enhanced [O IV] emission (e.g.,

Schaerer & Stasińska 1999). And maybe a decreased PAH equivalent width results from a relatively low ratio of photo-dissociation region to H II region contributions (Laurent et al. 2000).

The dotted lines in Figure 3 represent a variable mix of an AGN nucleus and a "pure" star-forming H II region. The 100% AGN anchor for these mixing models have values of EW(PAH 6.2 μm)= 0.01 μm, [O IV]25.89 μm/[Ne II]12.81 μm=0.3, and [Si II]34.82 μm/[Ne II]12.81 μm=2, whereas the 100% star formation anchor has EW(PAH 6.2 μm)$\sim$0.7 μm, [O IV]25.89 μm/[Ne II]12.81 μm=0.01, and [Si II]34.82 μm/[Ne II]12.81 μm=0.4. The dashed line in the upper panel of Figure 3 shows the approximate mixing model of Genzel et al. (1998), obtained after empirically deriving a relation between their 7.7 μm PAH 'strength' (line-to-continuum ratio) and the 6.2 μm PAH equivalent width. Many of the high ionization line data presented in Genzel et al. (1998) were upper limits, so it is unsurprising that their original curve lies above our curve. Short solid lines roughly perpendicular to the dotted AGN/star-forming curves delineate three regions in both panels of Figure 3. The boundaries are:

$$\text{Region[I} - \text{ II]} : \log([\text{O IV}]25.89\mu\text{m}/[\text{Ne II}]12.81\mu\text{m}) = 10 \ \log(\text{EW}[6.2\mu\text{mPAH}]) + 8.0 \quad (1)$$

$$\text{Region[II} - \text{III]} : \log([\text{O IV}]25.89\mu\text{m}/[\text{Ne II}]12.81\mu\text{m}) = 3.4\log(\text{EW}[6.2\mu\text{mPAH}]) - 0.2 \quad (2)$$

$$\text{Region[IV} - \text{V]} : \log([\text{Si II}]34.82\mu\text{m}/[\text{Ne II}]12.81\mu\text{m}) = 5.0\log(\text{EW}[6.2\mu\text{mPAH}]) + 4.8 \quad (3)$$

$$\text{Region[V} - \text{VI]} : \log([\text{Si II}]34.82\mu\text{m}/[\text{Ne II}]12.81\mu\text{m}) = 1.7\log(\text{EW}[6.2\mu\text{mPAH}]) + 0.5 \quad (4)$$

The population statistics for these regions, provided in Table 4, show that Regions [I+IV] and [III+VI] are respectively representative of Seyferts and star-forming systems. Regions [II+V], on the other hand, contain a mix of classifications and thus represent transition regions—either the source classifications in this region are ambiguous or the region simply contains a more heterogeneous mixture of pure types.

5.2.2. *Line Ratios from Atoms of Different Ionizations*

Figure 4 plots a ratio of doubly- to singly-ionized neon as a function of a ratio of triply- to doubly-ionized sulfur. Many of the data points in this plot are for Galactic H II regions (Vermeij et al. 2002; Giveon et al. 2002; Peeters et al. 2002; see § 3.2). Clearly the neon excitation tracks the sulfur excitation. To first order, there does not appear to be any sequence in the distribution according to source classification (Seyfert, starburst, H II, etc). However, the low-metallicity H II regions from the Magellanic Clouds are preferentially in the high excitation, upper righthand corner of the diagram. Presumably the diminished line blanketing for low-metallicity sources results in a harder radiation field and thus higher excitations (see Genzel & Cesarsky 2000; Martín-Hernández et al. 2002; Madden et al. 2005). In addition, AGN sources show somewhat lower [Ne III]15.6 μm/[Ne II]12.81 μm ratios, and the locus of the AGN detections lie at slightly higher values of [S IV]10.51 μm/[S III]18.71 μm. The dotted and solid curves show linear fits to the AGN and star-forming sources, respectively.

5.2.3.   A Neon, Sulfur, and Silicon Diagnostic

If the neon excitation is plotted as a function of [S III]33.48 μm/[Si II]34.82 μm (Figure 5), a more obvious separation of the star-forming and AGN-powered data points is observed. Not only do the low-metallicity Magellanic Cloud regions exhibit a higher neon excitation, nearly all of the "pure star-forming" nuclei and extra-nuclear regions show relatively elevated ratios in [S III]33.48 μm/[Si II]34.82 μm. Note in addition that many of the filled squares representing starbursting/star-forming nuclei are located between the H II regions and the AGN. Table 5 quantifies the source type fractions within each of the four regions delineated by the lines drawn in Figure 5. The boundaries are defined by curves with the same slope but differing offsets:

$$\log([\text{Ne III}]15.56\mu\text{m}/[\text{Ne II}]12.81\mu\text{m}) = 8.4\log([\text{S III}]33.48\mu\text{m}/[\text{Si II}]34.82\mu\text{m}) + \gamma, \qquad (5)$$

where $\gamma = [+3.3, +1.2, -2.5]$ for the lines demarcating Regions [I−II,II−III,III−IV].

These results can be partially understood in the context of the cooling line physics introduced above. The [Si II]34.82 μm line is a significant coolant of X-ray ionized regions or photo-dissociation regions (Hollenbach & Tielens 1999), whereas the [S III]33.48 μm line is a strong marker of H II regions. In other words, extra-nuclear regions and star-forming nuclei will show strong signatures of the Strömgren sphere coolant [S III]33.48 μm, while AGN and their associated X-ray dominated regions or dense photo-dissociation regions will exhibit relatively strong [Si II]34.82 μm emission in analogy to the increased strength of [O I] 6300Å emission in AGN (e.g., Veilleux & Osterbrock 1987). In addition, the fraction of photo-dissociation regions falling within each beam will play a role in the line ratios. The data for Magellanic Cloud and Galactic H II regions stem from smaller physical apertures and thus are likely to have fractionally higher contributions from Strömgren spheres than photo-dissociation regions.

Metallicity may be a factor as well. Since the central regions of galaxies typically are more abundant in heavy metals (Pagel & Edmunds 1981; McCall 1982; Vila-Costas & Edmunds 1992; Pilyugin & Ferrini 1998; Henry & Worthey 1999), and as explained above a lower metallicity can lead to harsher radiation fields and thus enhanced high-ionization-to-low-ionization line ratios, it is possible that this AGN→H II nucleus→H II region sequencing along the [S III]33.48 μm/[Si II]34.82 μm axis is affected by metallicity. However, the lower metallicity Magellanic Cloud data are not substantially to the right of the Galactic H II region data, so the effect is not solely due to metallicity. Alternatively, perhaps some of the star-forming nuclei have contributions from undetected weak AGN and thus are not "pure" star-forming nuclei, resulting in a location for star-forming nuclei on this diagram between AGN and H II regions.

5.2.4.   Density Diagnostics

The average line ratio of [S III]18.71 μm-to-[S III]33.48 μm for the SINGS sample is 0.82 with a 1σ dispersion of 0.27. This ratio implies an interstellar electron density of $\langle n_{\text{e}} \rangle \sim 400^{+240}_{-290}$ cm^{-3}

for the $\sim 23''\times15''$ nuclear and extranuclear regions of SINGS galaxies. The average density is calculated using electron collision strengths from Tayal & Gupta (1999). This density is typical of starburst/LINER/Seyfert galaxies (Kewley et al. 2001), and lower than the $\sim 10^3 - 10^4$ cm^3 expected from pure H II regions uncontaminated by the surrounding neutral interstellar medium (Wang et al. 2004). A visual way to explore this doubly-ionized sulfur line ratio is portrayed in Figure 6 using the aperture-matched 24 μm flux as a normalization for the line fluxes. The set of dashed lines represent different interstellar electron densities. The correlation in Figure 6 extends over two orders of magnitude in the line-to-continuum ratios and encompasses both AGN-dominated and star-formation-dominated sources; a non-parametric ranking analysis indicates a global correlation at the 7σ level. Linear fits to the two separate populations emphasize that, though the trends for the two populations are similar, the nuclei with Seyfert or LINER characteristics (dotted line) differ *along the diagonal* from the starbursting nuclei and the H II regions (solid line). Star-forming sources show more pronounced [S III]33.48 μm-to-continuum ratios compared to Seyferts and LINERs, consistent with the notion that [S III]33.48 μm is an important coolant of H II regions. Alternatively, we are seeing the effects of continuum dilution in the line-to-continuum ratio for Seyferts and LINERs, sources for which hot dust emission is pronounced in the mid-infrared and thus the line-to-continuum ratios are suppressed (e.g., Laurent et al. 2000; Dale et al. 2001; Xu et al. 2001; Siebenmorgen et al. 2004). Finally, similar to what is seen in Figures 3 and 5, but perhaps not as prominently, the data in Figure 6 suggest that the H II regions (open squares) occupy a different portion of the diagram than star-forming nuclei (filled squares). H II regions have higher line-to-continuum ratios than star-forming nuclei, which in turn have higher ratios than Seyferts and LINERs.

6. Summary

We have presented mid-infrared diagnostic diagrams for a large portion of the SINGS sample supplemented by archival *ISO* and *Spitzer* data. A portion of our work solidifies and extends previous *ISO*-based mid-infrared work to lower luminosity normal galaxy nuclei and H II regions using the *Spitzer Space Telescope*. We also present new diagnostics that effectively constrain a galaxy's dominant power source. The power of the diagnostic diagrams of Genzel et al. (1998; see also Peeters, Spoon, & Tielens 2004) for distinguishing between AGN and star-forming sources in dusty ULIRGs is that mid-infrared lines and PAH features are much less affected by extinction than their optical counterparts in a traditional diagnostic diagram. Unlike diagrams put forth by Genzel et al., which rely on detecting relatively weak high-ionization lines like [O IV] 25.89 μm and [Ne V] 14.32 μm, we provide a new diagnostic that utilizes a strong *low*-ionization line. The advantage of using a line ratio like [Si II]/[Ne II] is that singly-ionized silicon and neon respectively have ionization potentials of only 8.15 and 12.8 eV, so they can both be observed over a large range of physical conditions. This is similar in concept to previous efforts that have taken advantage of [O I] lines (e.g., at 6300 Å or 63 μm) that are coolants of the X-ray dominated regions (or dense photodissociation regions) surrounding AGN. In plots of both [O IV]/[Ne II] vs PAH and

[Si II]/[Ne II] vs. PAH we identify a region where $\gtrsim 90\%$ of the sources are Seyfert or LINER. Likewise, another region in both plots is $\gtrsim 90\%$ H II regions or star-forming nuclei.

Another useful mid-infrared diagnostic is [Ne III] 15.56 μm/[Ne II] 12.81 μm vs. [S III] 33.48 μm/[Si II] 34.82 μm. This plot tracks the excitation power of the radiation field on one axis, while the other axis is a relative measure of the cooling of H II regions and X-ray dominated regions (or dense photo-dissociation regions). Similar to what is found for the [Si II]/[Ne II] vs. PAH diagnostic alluded to above, both starbursting nuclei and extranuclear regions stand apart from nuclei that are pow-ered by accretion-powered disks. Moreover, compared to starbursting nuclei, extranuclear regions typically separate even further from Seyfert nuclei, especially for low-metallicity environments. Presumably this extranuclear$\longleftrightarrow$nuclear separation occurs since extranuclear regions are cleaner representatives of H II regions than starburst nuclei, because their stellar populations and inter-stellar medium structure are less complex. Extranuclear regions more likely contain younger stellar populations since they trace a single burst, as opposed to the average of multiple star formation episodes for nuclei (e.g., Dale et al. 2004b). Finally, we note that it is difficult to clearly distinguish between pure Seyfert and pure LINER sources using these diagnostics.

The line ratio [S III] 18.71 μm/[S III] 33.48 μm yields an average interstellar electron density of $\langle n_{\rm e} \rangle \sim 400^{+240}_{-290}$ cm^{-3} for the $\sim 23'' \times 15''$ nuclear and extranuclear regions of SINGS galaxies. This density is much closer (in log space) to the theoretical low density limit of Tayal & Gupta (1999) than their high density limit, and in fact the data for several sources are consistent with the low density limiting value. In addition to the interstellar gas densities being unremarkable, there are no SINGS sources sufficiently obscured by dust such that optical and infrared diagnostics provide obviously discrepant classifications of the energy source. This is not surprising, however, since our nuclei exhibit modest extinctions, $\langle A_V \rangle \sim 1.0$ mag, and normal star-forming galaxy nuclei in general show $0 \lesssim A_V \lesssim 3$ mag (Ho, Filippenko, & Sargent 1997). This relative transparency means the SINGS sample is not ideally suited for a detailed comparison of the relative merits of optical and infrared classifications. However, the diverse SINGS sample of nuclear and extranuclear regions provides an enormous range of physical parameters, and this has proved useful in developing the mid-infrared diagnostics in this paper.

REFERENCES

Armus, L., Heckman, T.M., & Miley, G.K. 1989, ApJ, 347, 727

Armus, L. et al. 2004, ApJS, 154, L178

Baldwin, J.A., Phillips, M.M., & Terlevich, R. 1981, PASP, 93, 5

Cesarsky, D., Lequeux, J., Abergel, A., Perault, M., Palazzi, E., Madden, S., & Tran, D. 1996, A&A, 315, L309

Dale, D.A., Helou, G., Contursi, A., Silbermann, N.A., & Kolhatkar, S. 2001, ApJ, 549, 215

Dale, D.A., Helou, G., Brauher, J.R., Cutri, R.M., Malhotra, S., & Beichman, C.A. 2004a, ApJ, 604, 565

Dale, D.A. et al. 2004b, ApJ, 601, 813

Dale, D.A. et al. 2005, ApJ, 633, 857

Draine, B.T. & Li, A. 2001, ApJ, 551, 807

Engelbracht, C.W., Gordon, K.D., Rieke, G.H., Werner, M.W., Dale, D.A., & Latter, W.B. 2005, ApJ, 628, L29

Förster Schrieber, N.M., Roussel, H., Sauvage, M., & Charmandaris, V. 2004, A&A, 419, 501

Galliano, F., Madden, S.C., Jones, A.P., Wilson, C.D., & Bernard, J.-P. 2005, A&A, 434, 867

Genzel, R. et al. 1998, ApJ, 498, 579

Genzel, R. & Cesarsky, C.J. 2000, ARA&A, 38, 761

Giveon, U., Sternberg, A., Lutz, D., Feuchtgruber, H., & Pauldrach, A.W.A. 2002, ApJ, 566, 880

Haas, M., Siebenmorgen, R., Schulz, B., Krügel, E., & Chini, R. 2005, A&A, in press

Henry, R.B.C. & Worthey, G. 1999, PASP, 111, 919

Ho, L., Filippenko, A.V., & Sargent, W.L. 1993, ApJ, 417, 63

Ho, L., Filippenko, A.V., & Sargent, W.L. 1997, ApJ, 487, 579

Hollenbach, D. & Tielens, A.G.G.M. 1999, Rev. Mod. Phys., 71, 173

Houck, J.R. et al. 2004a, ApJS, 154, L18

Houck, J.R. et al. 2004b, ApJS, 154, L211

Kauffmann, G. et al. 2003, MNRAS, 346, 1055

Kennicutt, R.C. et al. 2003, PASP, 115, 928

Kewley, L.J., Dopita, M.A., Sutherland, R.S., Heisler, C.A., Trevena, J. 2001, ApJ, 556, 121

Laurent, O., Mirabel, I.F., Charmandaris, V., Gallais, P., Madden, S.C., Sauvage, M., Vigroux, L., & Cesarsky, C. 2000, A&A, 359, 887

Li, A. & Draine, B.T. 2001, ApJ, 554, 778

Madden, S.C., Galliano, F., Jones, A.P., & Sauvage, M. 2005, A&A, in press (astro-ph/0510086)

Maloney, P.R., Hollenbach, D.J., & Tielens, A.G.G.M. 1996, ApJ, 466, 561

Martín-Hernández, N.L., Vermeij, R., Tielens, A.G.G.M., van der Hulst, J.M., & Peeters, E. 2002, A&A, 389, 286

McCall, M.L. 1982, Ph.D. thesis, University of Texas at Austin

Meijerink, R. & Spaans, M. 2005, A&A, 436, 397

Moustakas, J. & Kennicutt, R.C. 2006, ApJ, in press (astro-ph/0511729)

Osterbrock, D.E. 1993, ApJ, 404, 551

Pagel, B.E.J. & Edmunds,M.G. 1981, ARA&A, 19, 77

Peeters, E. et al. 2002, A&A, 381, 571

Peeters, E., Spoon, H.W.W., & Tielens, A.G.G.M. 2004, ApJ, 613, 986

Peeters, E., Mattioda, A.L., Hudgins, D.M., & Allamandola, L.J. 2004, ApJ, 617, L65

Pilyugin, L.S. & Ferrini, F. 1998, A&A, 336, 103

Rieke, G.H. et al. 2004, ApJS, 154, 25

Roussel, H., Helou, G., Beck, R., Condon, J.J., Bosma, A., Matthews, K., & Jarrett, T.H. 2003, ApJ, 593, 733

Schaerer, D. & Stasińska, G. 1999, A&A, 345, L17

Siebenmorgen, R., Freudling, W., Krügel, E., & Haas, M., 2004, A&A, 421, 129

Smith, J.D.T. et al. 2004, ApJS, 154, L199

Spinoglio, L. & Malkan, M.A. 1992, ApJ, 399, 504

Sturm, E., Lutz, D., Tran, D., Feuchtgruber, H., Genzel, R., Kunze, D., Moorwood, A.F.M., & Thornley, M.D. 2000, A&A, 358, 481

Sturm, E., Lutz, D., Verma, A., Netzer, H., Sternberg, A., Moorwood, A.F.M., Oliva, E., & Genzel, R. 2002, A&A, 393, 821

Taniguchi, Y., Yoshino, A., Ohyama, Y., & Nishiura, S. 1999, ApJ, 514, 660

Tayal, S.S., & Gupta, G.P. 1999, ApJS, 526, 544

Thornley, M.D., Förster Schreiber, N.M., Lutz, D., Genzel, R., Spoon, H.W.W., Kunze, D., & Sternberg, A. 2000, ApJ, 539, 641

Thuan, T.X., Sauvage, M., & Madden, S. 1999, ApJ, 516, 783

Tran, Q.D. et al. 2001, ApJ, 552, 527

Veilleux, S. & Osterbrock, D.E. 1987, ApJS, 63, 295

Veilleux, S. 1991, ApJ, 369, 331

Veilleux, S., Sanders, D.B., & Kim, D.-C. 1999, ApJ, 522, 139

Verma, A., Lutz, D., Sturm, E., Sternberg, A., Genzel, R., & Vacca, W. 2003, A&A, 403, 829

Vermeij, R. & van der Hulst, J.M. 2002, A&A, 391, 1081

Vermeij, R., Damour, F., van der Hulst, J.M., & Baluteau, J.-P. 2002, A&A, 390, 649

Verstraete, L., Pech, C., Moutou, C., Sellgren, K., Wright, C.M., Giard, M., Léger, A., Timmerman, R., & Drapatz, S. 2001, A&A, 372, 981

Vila-Costas, M.B. & Edmunds, M.G. 1992, MNRAS, 259, 121

Voit, G.M. 1992, ApJ, 399, 495

Wang, W., Liu, X.-W., Zhang, Y., & Barlow, M.J. 2004, A&A, 427, 873

Weedman, D.W., Hao, L., Higdon, S.J.U., Devost, D., Wu, Y., Charmandaris, V., Brandl, B., Bass, E., & Houck, J.R. 2005, ApJ, 633, 706

Xu, C., Lonsdale, C.J., Shupe, D.L., O'Linger, J., & Masci, F. 2001, ApJ, 562, 179

Table 1.   Nuclear Emission Line Fluxes and 6.2 μm PAH Feature Equivalent Widths

Species Wavelength ionization (eV)	PAH 6.2μm	[SIV] 10.51μm 34.8	[NeII] 12.81μm 21.6	[NeIII] 15.56μm 41.0	[SIII] 18.71μm 23.3	[OIV] 25.89μm 54.9	[SIII] 33.48μm 23.3	[SiII] 34.82μm 8.2
NGC 0337	0.56±0.04	⋯	17.4±1.6	8.1±0.5	13.3±0.6	0.5±0.2	17.9±0.5	21.1±0.6
NGC 0584	⋯	⋯	⋯	2.4±0.7	1.1±0.5	<0.8	⋯	⋯
NGC 0628	0.39±0.08	⋯	6.4±1.3	⋯	2.5±0.3	<0.7	9.1±0.7	5.8±0.8
NGC 1097	0.42±0.01	⋯	328±4	29.0±0.6	89.6±0.5	<5.3	103±3	278±4
NGC 1266	0.29±0.02	⋯	28.0±1.0	10.8±0.6	1.3±0.5	<2.8	2.7±0.6	17.3±3.7
NGC 1377	⋯	⋯	⋯	⋯	⋯	<3.4	⋯	⋯
NGC 1404	⋯	⋯	1.9±0.8	1.3±0.6	⋯	<0.7	⋯	⋯
NGC 1566	0.20±0.01	1.1±0.6	16.6±0.8	9.8±0.4	6.8±0.6	6.7±0.5	6.8±0.7	15.2±0.8
NGC 1705	0.42±0.26	3.2±0.8	1.1±0.3	7.0±0.4	3.4±0.4	1.2±0.4	4.9±0.5	3.6±0.5
NGC 2798	0.52±0.02	5.9±1.8	208±2	34.4±0.5	81.6±0.8	9.6±1.8	70.1±2.6	102±4
NGC 2841	0.03±0.03	⋯	5.5±0.5	6.6±0.4	2.7±0.5	0.9±0.1	3.6±0.4	9.7±2.3
NGC 2915	⋯	1.8±0.9	3.1±0.4	11.1±0.4	4.6±0.4	0.4±0.1	6.1±0.8	4.9±0.4
NGC 2976	0.35±0.04	⋯	7.7±0.7	2.7±0.3	6.3±0.4	0.4±0.1	9.2±0.3	8.5±0.5
NGC 3049	0.62±0.04	1.1±0.6	36.4±0.8	6.1±0.4	27.3±0.6	<0.7	24.4±0.4	21.5±0.5
NGC 3190	0.09±0.01	⋯	7.4±0.6	5.6±0.5	1.8±0.6	0.7±0.2	2.0±0.2	6.9±1.7
NGC 3184	0.26±0.04	⋯	17.8±0.5	2.1±0.5	7.8±0.5	<0.7	7.2±0.3	12.0±0.4
NGC 3198	0.31±0.03	⋯	13.9±0.4	0.8±0.3	4.8±0.5	<0.9	5.5±0.5	11.1±2.2
NGC 3265	0.57±0.03	1.5±0.7	28.4±0.3	4.9±0.2	11.7±0.3	<1.2	13.1±0.6	16.9±0.7
Markarian 33	0.51±0.02	17.1±0.8	56.7±1.1	45.3±0.4	42.8±0.7	1.0±0.7	32.8±0.8	25.1±0.9
NGC 3351	0.46±0.01	⋯	165±2	14.0±0.4	60.0±0.5	<2.3	60.5±1.7	128±2
NGC 3521	0.38±0.04	⋯	12.9±0.8	7.9±0.5	3.3±0.7	0.8±0.4	3.6±0.8	16.7±2.3
NGC 3627	0.25±0.01	⋯	21.9±0.9	8.9±0.5	4.7±0.4	1.3±0.7	7.0±1.1	20.2±3.3
NGC 3773	0.65±0.08	3.9±0.7	16.5±0.5	16.1±0.5	14.3±0.6	<0.8	17.0±0.6	13.1±0.7
NGC 3938	0.13±0.03	⋯	5.7±0.5	1.0±0.5	1.1±0.5	0.3±0.1	2.2±0.1	5.9±0.2
NGC 4125	⋯	⋯	2.5±0.5	3.4±0.5	⋯	<0.9	0.8±0.6	5.4±1.1
NGC 4254	0.54±0.03	⋯	51.7±1.1	6.4±0.4	10.0±0.5	1.3±0.2	15.6±0.6	48.9±1.1
NGC 4321	0.49±0.02	⋯	110±2	12.3±0.4	23.1±0.3	<1.4	25.5±0.8	84.8±0.9
NGC 4536	0.54±0.01	7.5±2.6	307±3	48.9±0.7	130±1	<3.9	160±3	220±3
NGC 4552	⋯	⋯	1.8±0.5	4.8±0.8	0.9±0.4	<0.9	0.7±0.3	2.0±0.7
NGC 4569	0.26±0.02	1.0±0.8	32.6±1.2	15.8±0.5	8.8±0.7	2.4±0.6	7.7±0.6	31.5±0.9
NGC 4579	0.09±0.02	⋯	22.8±0.7	12.5±0.5	4.0±0.7	2.2±0.3	3.0±0.4	19.5±0.4
NGC 4725	0.07±0.04	0.8±0.5	1.8±0.5	3.0±0.4	0.3±0.2	1.7±0.2	1.3±0.2	4.6±1.5
NGC 4736	0.16±0.01	⋯	13.7±1.1	14.3±0.5	6.1±0.9	3.8±0.9	9.2±1.0	22.3±1.8
NGC 4826	0.28±0.01	1.8±0.5	99.0±1.6	23.4±0.6	41.8±0.4	2.5±1.1	56.8±1.0	105±1
NGC 5194	0.24±0.02	2.9±0.8	66.2±0.8	36.2±0.6	13.1±0.6	14.9±1.6	18.3±0.4	64.8±0.8
NGC 5408[a]	⋯	⋯	⋯	1.7±0.4	⋯	<0.9	1.5±0.5	1.8±0.5
NGC 5713	0.56±0.02	1.7±0.7	123±2	17.3±0.4	47.5±0.5	2.0±1.0	57.2±1.2	90.3±1.2
NGC 5866	0.07±0.01	⋯	7.5±0.9	5.1±0.3	1.1±0.4	0.7±0.1	4.0±0.3	9.7±0.4
IC 4710	⋯	3.6±0.8	⋯	4.3±1.6	3.6±0.5	<1.3	4.2±0.6	1.4±0.4
NGC 7331	0.09±0.02	0.5±0.2	18.8±0.6	10.3±0.3	6.0±0.4	2.4±0.6	12.2±0.3	29.0±0.5
NGC 7552	0.45±0.01	6.5±1.4	573±31	56.8±1.4	211±1	<15.3	165±5	260±8
NGC 7793	0.36±0.04	⋯	10.3±0.6	2.9±0.5	8.7±0.6	<0.5	9.4±0.3	9.5±0.5

Note. — Fluxes and their (statistical) uncertainties are listed in units of 10^{-9} W m^{-2} sr^{-1}. Calibration uncertainties are an additional ∼30%. The 6.2 μm PAH feature equivalent width is given in units of microns.

[a]The infrared emission peaks outside of the field of view of the spectral maps.

Table 2.   Extranuclear Emission Line Fluxes and 6.2 μm PAH Feature Equivalent Widths

Species Wavelength ionization (eV)	PAH 6.2μm	[SIV] 10.51μm 34.8	[NeII] 12.81μm 21.6	[NeIII] 15.56μm 41.0	[SIII] 18.71μm 23.3	[OIV] 25.89μm 54.9	[SIII] 33.48μm 23.3	[SiII] 34.82μm 8.2
NGC 5194 CCM107	0.47±0.02	$\cdots$	32.0±0.6	2.3±0.6	10.6±0.5	1.7±0.3	18.3±0.5	34.1±0.5
NGC 5194 CCM072	0.61±0.02	1.7±0.5	71.9±1.0	3.8±0.4	29.4±0.6	1.4±0.8	36.2±0.5	49.2±0.7
NGC 5194 CCM071	0.66±0.02	$\cdots$	44.3±0.7	5.6±0.5	16.6±0.7	1.3±0.4	25.0±0.6	41.2±0.5
NGC 5194 CCM001	0.69±0.02	$\cdots$	16.4±1.1	3.3±0.5	19.8±0.5	0.6±0.2	13.7±0.5	21.7±0.9
NGC 5194 CCM010	0.69±0.03	$\cdots$	39.2±0.7	6.1±0.4	19.8±0.5	0.5±0.3	29.0±0.5	37.7±0.7
NGC 5194 CCM071A	0.52±0.02	$\cdots$	21.3±0.6	5.7±0.4	11.0±0.5	<0.6	14.4±2.1	12.6±0.4
NGC 3031 HK230	0.44±0.03	$\cdots$	4.1±0.5	0.7±0.5	2.7±0.4	<0.7	3.6±0.5	4.0±0.4
NGC 3031 HK343	0.38±0.03	$\cdots$	7.5±3.1	3.6±0.4	7.0±0.9	<0.8	9.8±0.8	7.0±0.6
NGC 3031 HK453	0.65±0.05	$\cdots$	9.0±0.6	3.4±0.4	8.8±0.9	<0.8	11.7±2.0	9.3±0.6
NGC 3031 HK268	0.55±0.03	1.2±0.7	15.1±0.8	6.0±0.4	13.4±0.7	<0.8	17.3±0.7	13.0±0.6
NGC 3031 HK652	0.68±0.06	$\cdots$	10.3±0.7	2.7±0.5	9.2±1.1	<0.8	10.7±0.8	11.8±0.6
NGC 3031 HK741	0.75±0.05	$\cdots$	8.9±0.8	1.6±0.4	7.3±0.4	<0.9	7.6±0.7	6.5±0.7
NGC 3031 Munch1	2.98±2.29	$\cdots$	$\cdots$	1.4±0.2	$\cdots$	<1.0	$\cdots$	$\cdots$
NGC 6946 H4	0.65±0.02	3.6±0.7	16.6±0.6	17.5±0.5	14.7±0.4	1.1±0.2	14.2±0.6	14.6±0.5
NGC 6946 HK3	0.63±0.03	8.8±1.3	28.2±0.4	31.9±0.4	30.6±0.4	0.9±0.2	39.0±0.5	25.1±0.5
NGC 6946 H288	0.81±0.04	$\cdots$	18.1±0.4	8.5±0.4	14.0±0.5	<0.6	19.3±0.3	11.8±0.2
NGC 6946 H40	0.84±0.03	1.9±0.8	18.8±0.4	8.5±0.4	15.0±0.4	0.2±0.1	17.3±0.3	15.2±0.5
NGC 6946 H28	1.05±0.45	$\cdots$	9.4±0.5	2.9±0.3	6.8±0.5	<0.5	9.0±0.3	8.2±0.4
NGC 0628 H292	0.55±0.02	2.1±0.9	25.6±0.7	2.7±0.4	20.1±0.6	<1.0	27.4±0.5	13.1±0.7
NGC 0628 H572	0.69±0.03	$\cdots$	12.5±0.7	2.6±0.5	8.1±0.4	<0.9	16.3±0.5	8.2±0.6
NGC 0628 H627	0.60±0.03	3.8±1.3	11.5±0.7	9.5±0.5	10.6±0.4	<0.9	17.8±0.9	9.6±0.5
NGC 0628 H013	0.52±0.07	$\cdots$	4.1±0.7	2.2±0.3	4.9±0.4	<0.7	11.3±1.3	2.9±0.4
HolmbergII HSK45	$\cdots$	$\cdots$	$\cdots$	3.4±0.5	3.2±0.4	<0.9	2.9±0.7	2.8±0.5
HolmbergII HSK67	$\cdots$	$\cdots$	$\cdots$	0.7±0.2	$\cdots$	<0.7	0.6±0.2	0.9±0.3
HolmbergII HSK70	$\cdots$	$\cdots$	$\cdots$	1.1±0.5	0.6±0.2	<0.9	0.4±0.2	1.7±0.5
HolmbergII HSK07	$\cdots$	$\cdots$	$\cdots$	1.1±0.6	0.8±0.5	<1.0	$\cdots$	$\cdots$

Note. — Fluxes and their (statistical) uncertainties are listed in units of 10^{-9} W m^{-2} sr^{-1}. Calibration uncertainties are an additional ∼30%. The 6.2 μm PAH feature equivalent width is given in units of microns.

Table 3.   Archival Sources

Object	Type	Reference
LMC N160A1	LMC HII	Vermeij et al. (2002)
LMC N160A2	LMC HII	Vermeij et al. (2002)
LMC N159-5	LMC HII	Vermeij et al. (2002)
LMC N157B	LMC HII	Vermeij et al. (2002)
LMC N4A	LMC HII	Vermeij et al. (2002)
LMC N11A	LMC HII	Vermeij et al. (2002)
LMC N83B	LMC HII	Vermeij et al. (2002)
LMC 30Dor1	LMC HII	Vermeij et al. (2002)
LMC 30Dor2	LMC HII	Vermeij et al. (2002)
LMC 30Dor3	LMC HII	Vermeij et al. (2002)
LMC 30Dor4	LMC HII	Vermeij et al. (2002)
SMC N88A	SMC HII	Vermeij et al. (2002)
SMC N66	SMC HII	Vermeij et al. (2002)
SMC N81	SMC HII	Vermeij et al. (2002)
NGC 0253	HII nucleus	Verma et al. (2003)
IC 342	HII nucleus	Verma et al. (2003)
II Zw 40	HII nucleus	Verma et al. (2003)
NGC 3034	HII nucleus	Verma et al. (2003)
NGC 3256	HII nucleus	Verma et al. (2003)
NGC 3690A	HII nucleus	Verma et al. (2003)
NGC 3690B	HII nucleus	Verma et al. (2003)
NGC 4038	HII nucleus	Verma et al. (2003)
NGC 4945	HII/Seyfert	Verma et al. (2003)
NGC 5236	HII nucleus	Verma et al. (2003)
NGC 5253	HII nucleus	Verma et al. (2003)
NGC 7552	LINER/HII	Verma et al. (2003)
WB89 380 A	Galactic HII	Giveon et al. (2002)
WB89 380 B	Galactic HII	Giveon et al. (2002)
WB89 399	Galactic HII	Giveon et al. (2002)

Note. — The full version would appear as an electronic table in the online Journal.

Table 4.   Classifications by Region in Figure 3

Region	Number of Sources	Seyfert (%)	LINER (%)	HII nuclei (%)	extranuclear +HII regions (%)
I	15	73	20	7	0
II	32	41	22	22	16
III	30	0	10	33	57
IV	12	67	25	8	0
IV	39	33	18	21	28
IV	34	0	9	26	65

Note. — "extranuclear + HII regions" implies SINGS extranuclear/HII regions in addition to Milky Way and Magellanic Cloud HII regions.

Table 5.   Classifications by Region in Figure 5

Region	Number of Detections	Seyfert (%)	LINER (%)	HII nuclei (%)	extranuclear +HII regions (%)
I+II	38	61	32	8	0
III+IV	79	0	3	30	67
I	16	69	31	0	0
II	22	55	32	14	0
III	47	0	4	51	45
IV	32	0	0	0	100

Note. — "extranuclear + HII regions" implies SINGS extranuclear/HII regions in addition to Milky Way and Magellanic Cloud HII regions.
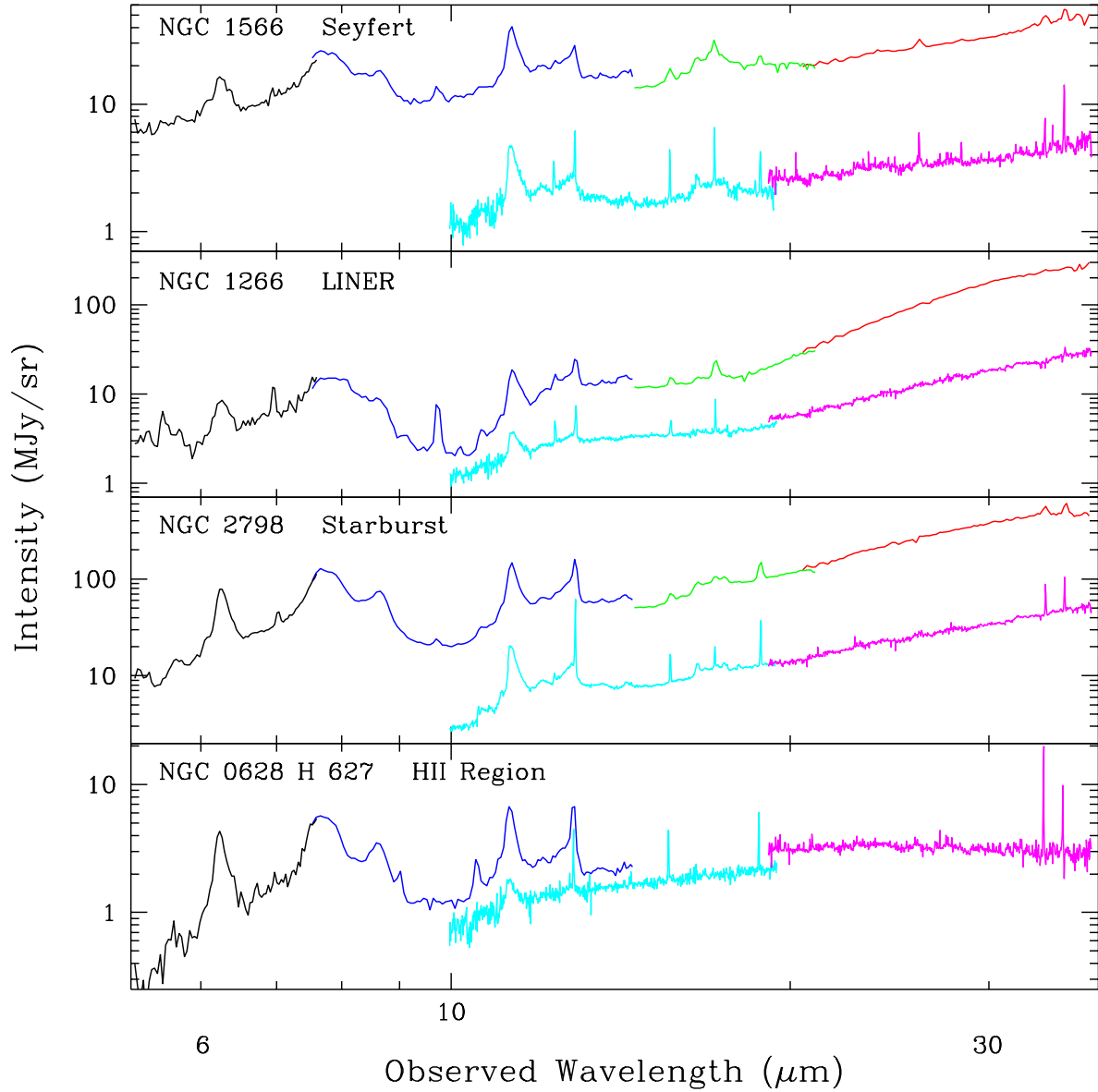
Fig. 1.— An example of both low- and high-resolution spectra for four different types of environments found within the SINGS sample. Each color corresponds to a different IRS module: black→Short-Low2, blue→Short-Low1, green→Long-Low2, red→Long-Low1, cyan→Short-High, and magenta→Long-High. Each spectral segment has been extracted from a ∼23″×15″ region. The low-resolution data are sky-subtracted, unlike the high-resolution data, which are scaled downwards by 1.0 dex for clarity.
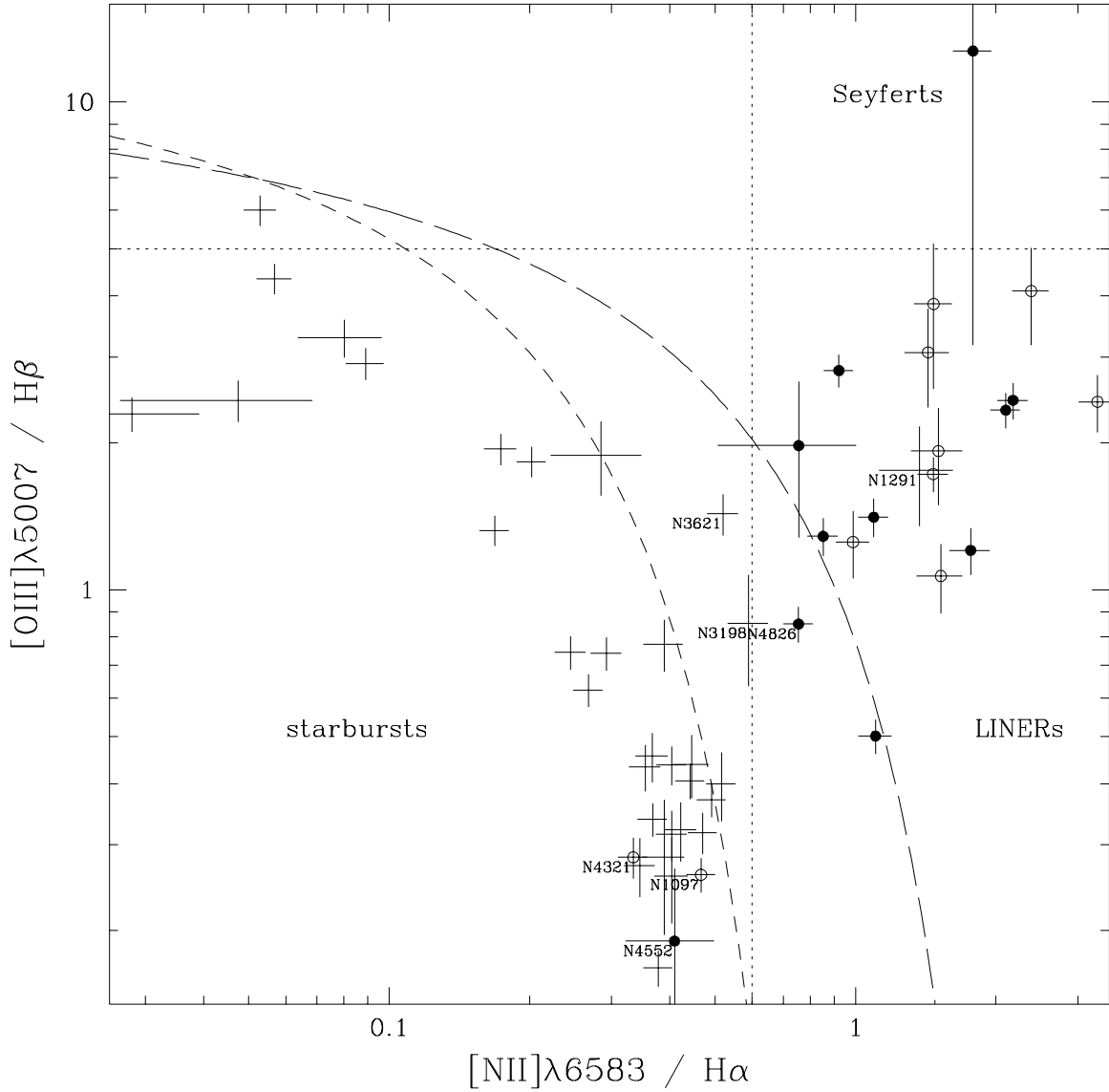
Fig. 2.— A traditional diagnostic diagram is displayed for the SINGS nuclei using optical data and $20'' \times 20''$ apertures (uncorrected for reddening). Filled (open) circles mark galaxies for which NED indicates a Seyfert (LINER) nucleus. The dotted lines delineate typical starburst/Seyfert/LINER boundaries: [O III]5007/H$\beta \sim 5$ and [N II]6583/H$\alpha \sim 0.6$ (e.g., Armus, Heckman, & Miley 1989). The long-dashed and short-dashed curves respectively trace the starburst/AGN boundaries of Kewley et al. (2001) and Kauffmann et al. (2003).
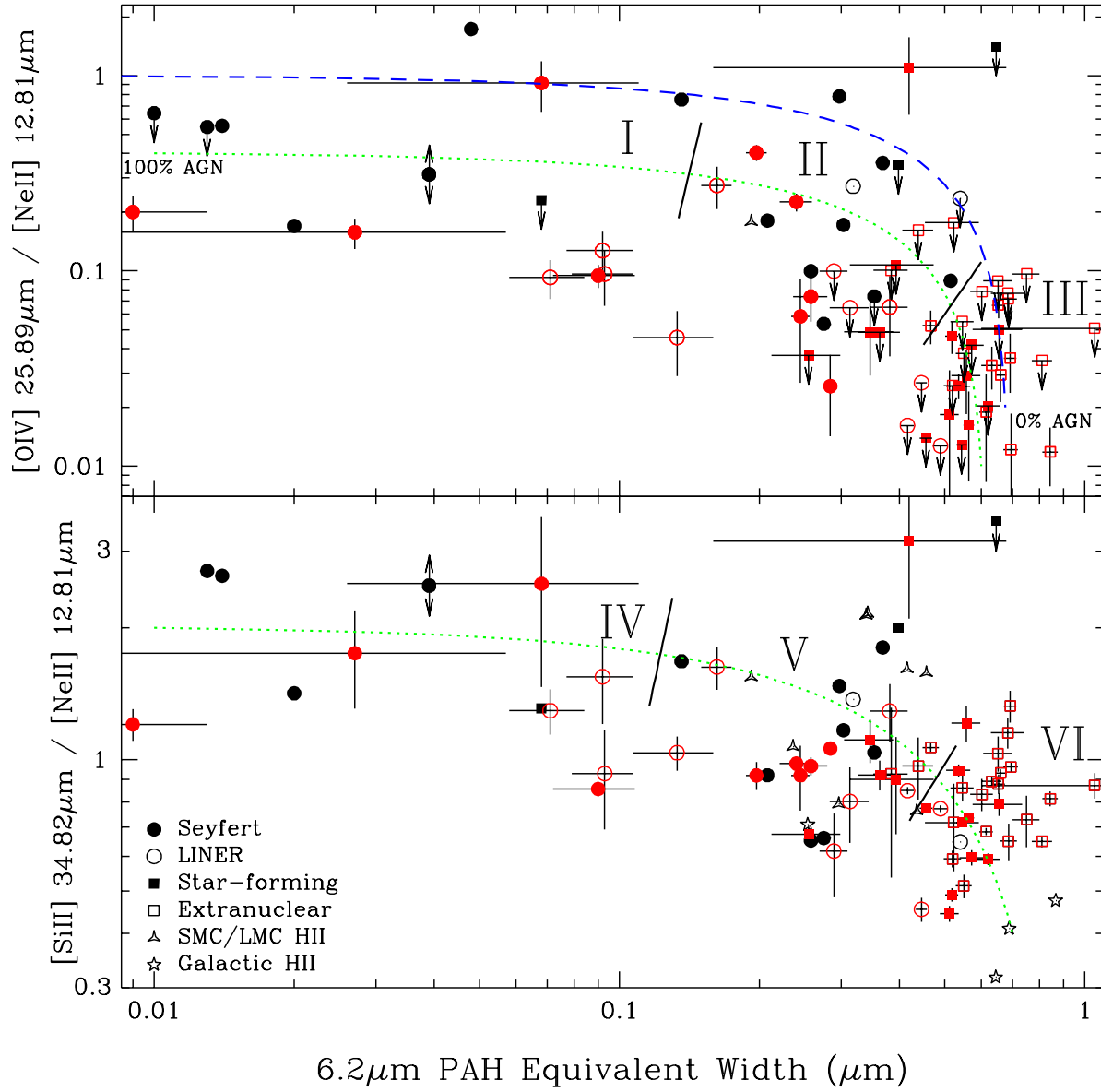
Fig. 3.— The ratios of mid-infrared forbidden lines as a function of the 6.2 μm PAH feature equivalent width. SINGS data are displayed in red with error bars based on the statistical uncertainties; archival data without error bars are indicated with black symbols and described in § 3.2. The dotted lines are linear mixing models of a "pure" AGN and a "pure" star-forming source (see text). The dashed line in the top panel is a similar mixing model first presented in Genzel et al. (1998).
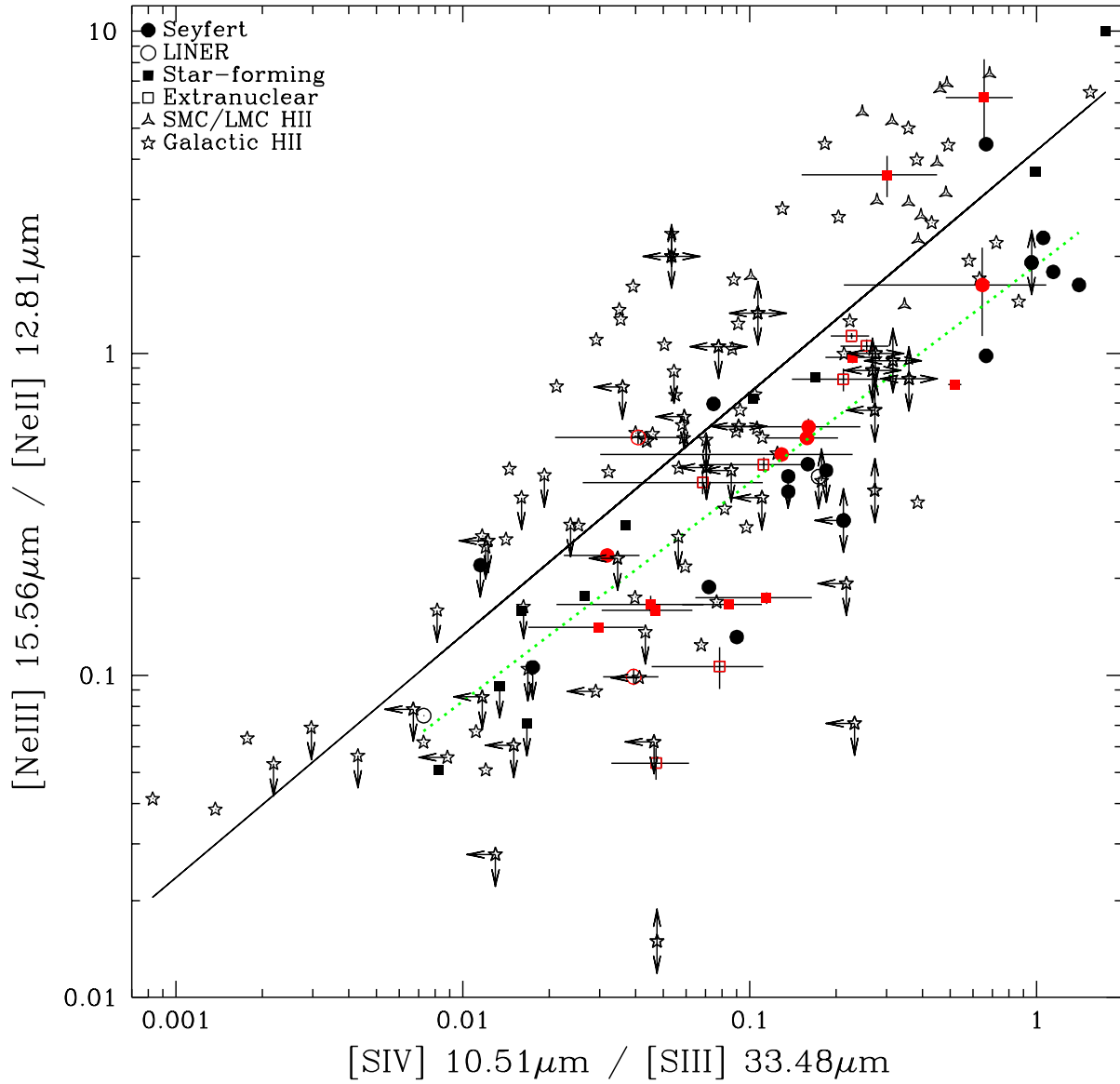
Fig. 4.— A diagnostic diagram involving ratios of neon and sulfur lines at different ionization levels is displayed. The data are displayed as described in Figure 3. The solid line is a linear fit to the detections of star-forming nuclei and H II regions, while the dotted line is linear fit to the Seyfert and LINER detections. Note how the data for the low metallicity Magellanic Clouds show very high excitation.
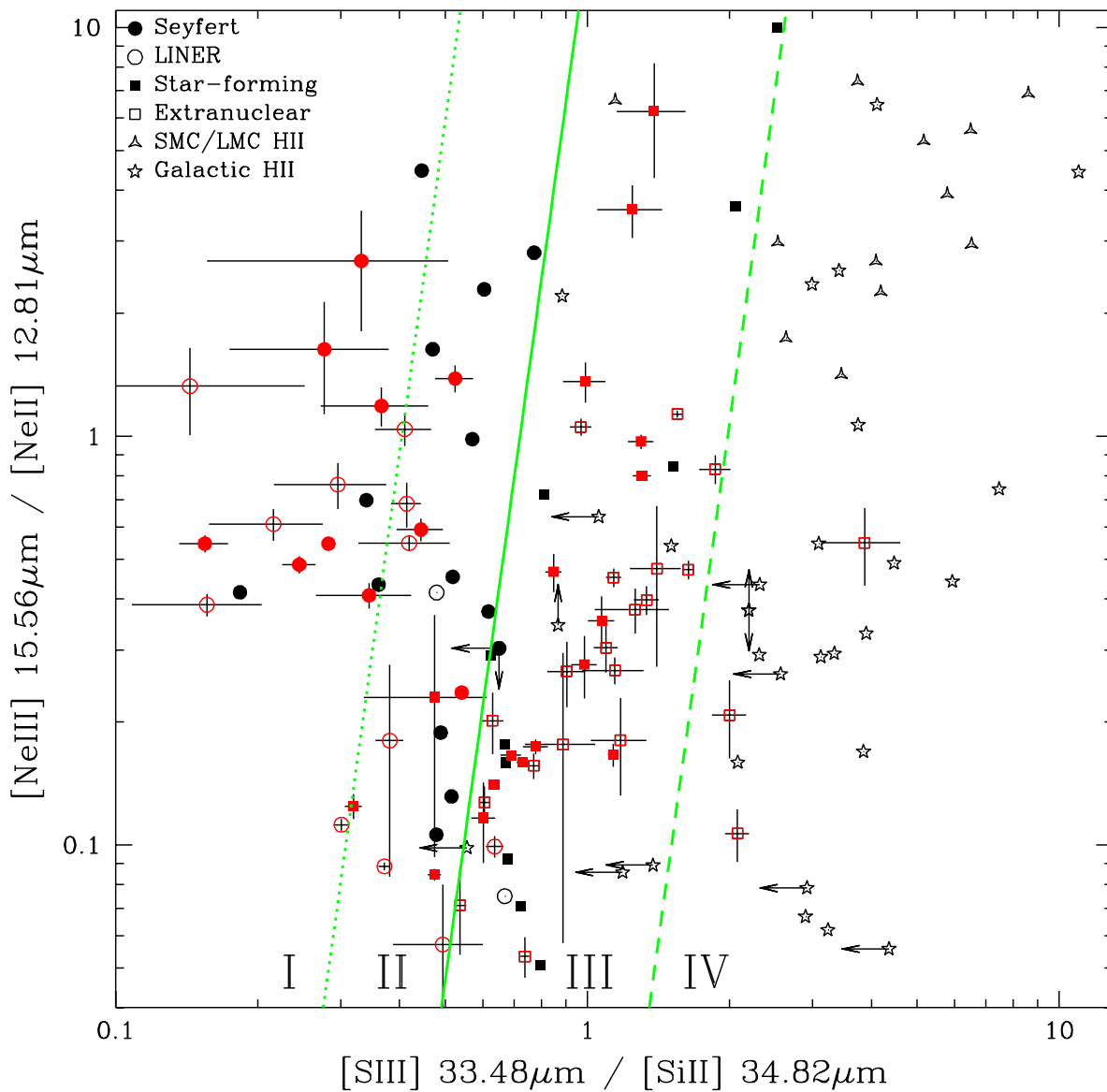
Fig. 5.— A neon, sulfur, and silicon diagnostic diagram involving ratios of lines at different ionizations is displayed. The data are displayed as described in Figure 3. The lines delineate regions distinguished by Seyferts/LINERs/starbursts/H II regions/etc (see Table 5 and § 5.2.3).
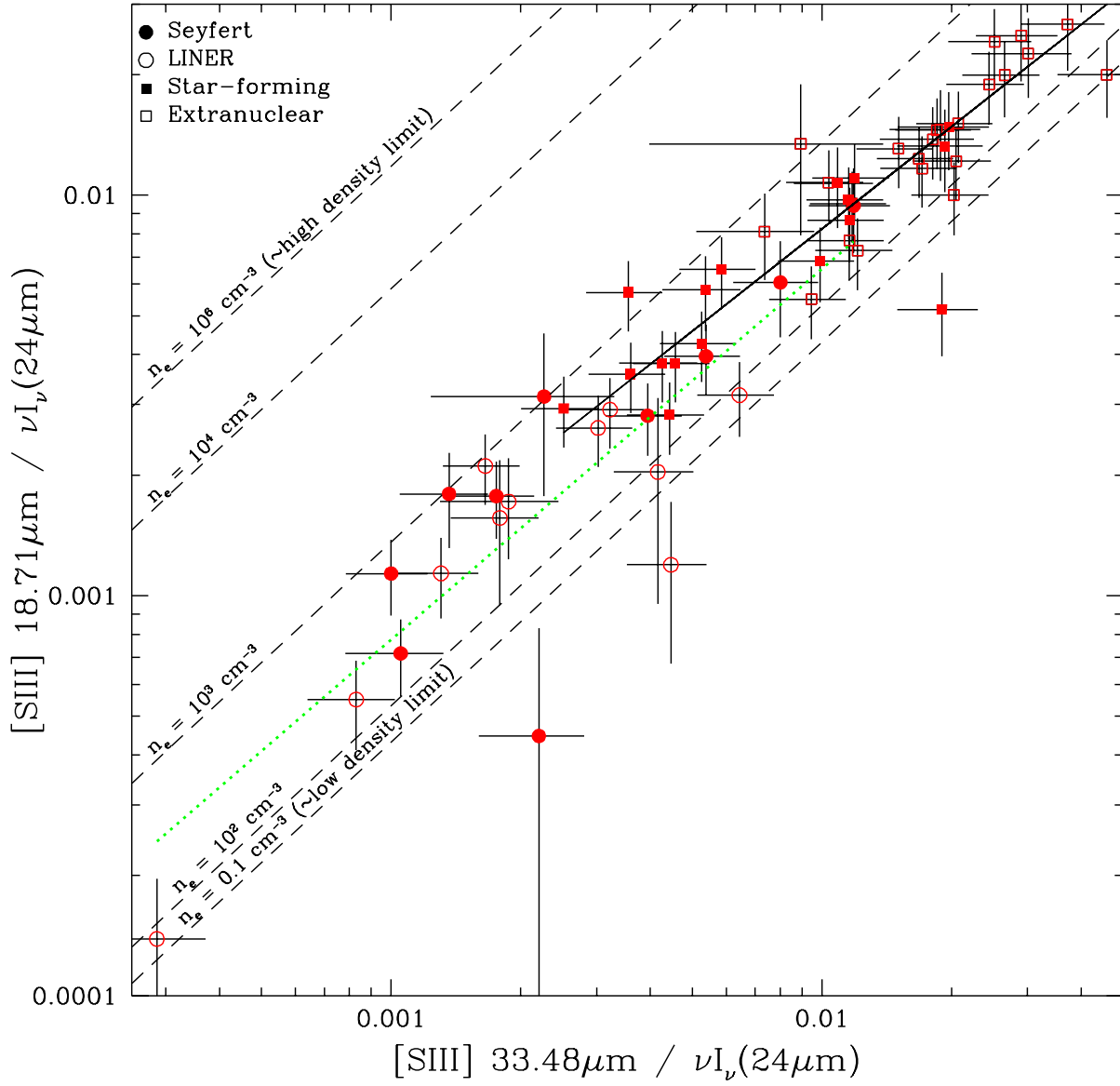
Fig. 6.— The correlation between two transitions of doubly-ionized sulfur is displayed, normalized by the flux at 24 μm. This plot includes only SINGS data. The solid line is a linear fit to the detections of star-forming nuclei and H II regions, while the dotted line is linear fit to the Seyfert and LINER detections. The set of dashed lines represent different constant interstellar electron densities. Most of the SINGS data are bounded by the low and high density limiting values, and several are consistent with the low density limiting value of [S III]18.71 μm/[S III]33.48 μm=0.43 at 0.1 cm^{-3}. The SINGS data typically exhibit $n_{\mathrm{e}} \sim 400$ cm^{-3}.